High-strength, porous additively manufactured implants with optimized mechanical osseointegration

Cambre N. Kelly [a], Tian Wang [b], James Crowley [b], Dan Wills [b], Matthew H. Pelletier [b], Edward R. Westrick [c], Samuel B. Adams [d], Ken Gall [a], William R. Walsh [b],*

[a] *Pratt School of Engineering, Duke University, Durham, NC, USA*
[b] *Surgical and Orthopaedic Research Laboratories (SORL), Prince of Wales Clinical School UNSW Sydney, Kensington, Australia*
[c] *Orthopedic Surgery, Allegheny General Hospital, Pittsburgh, PA, USA*
[d] *Department of Orthopedic Surgery, Duke University Medical Center, Durham, NC, USA*

ARTICLE INFO

ABSTRACT

Optimization of porous titanium alloy scaffolds designed for orthopedic implants requires balancing mechanical properties and osseointegrative performance. The tradeoff between scaffold porosity and the stiffness/strength must be optimized towards the goal to improve long term load sharing while simultaneously promoting osseointegration. Osseointegration into porous titanium implants covering a wide range of porosity (0%–90%) and manufactured by laser powder bed fusion (LPBF) was evaluated with an established ovine cortical and cancellous defect model. Direct apposition and remodeling of woven bone was observed at the implant surface, as well as bone formation within the interstices of the pores. A linear relationship was observed between the porosity and benchtop mechanical properties of the scaffolds, while a non-linear relationship was observed between porosity and the ex vivo cortical bone-implant interfacial shear strength. Our study supports the hypothesis of porosity dependent performance tradeoffs, and establishes generalized relationships between porosity and performance for design of topological optimized implants for osseointegration. These results are widely applicable for orthopedic implant design for arthroplasty components, arthrodesis devices such as spinal interbody fusion implants, and patient matched implants for treatment of large bone defects.

1. Introduction

Accelerating and maximizing the osseointegration of an orthopedic implant through modulation of implant topology has garnered increasing interest in recent years. With the ability to fabricate porous metallic scaffolds with increasing complexity, laser powder bed fusion (LPBF) has enabled a paradigm shift in the topological design of biomedical implants [1]. The integration of advanced computational design tools with LBPF, has unlocked engineering of porous scaffolds with prescribed properties and patient matched geometries. In fact, recent investigations into characterization of mechanical properties of AM titanium scaffolds with varied topologies and porosities show a wide range of resulting strengths and stiffnesses within the range of bone [2, 3]. Recent work has also demonstrated that triply periodic minimal surfaces (TPMS) sheet-based architectures, including the gyroid-sheet, exhibit favorable mechanical properties, by maintaining high strength and fatigue resistance relative to strut-based unit cell architectures of the

same porosity [3–6]. Additional topological design parameters such as the unit cell size, orientation, and even the ratio of the cell size to the overall porous volume impacts mechanical properties of porous scaffolds [2,4,7]. However, these topological design factors are all secondary to the dominating effect of scaffold porosity which drives the mechanical performance of the scaffold (strength and stiffness) and influences osseointegration [2–4].

By increasing the porosity of the titanium scaffold, the apparent modulus can be reduced to within the range of bone [2], however, there is also a correlated reduction in scaffold strength which must be balanced to support implantation and load bearing. Matching of implant stiffness to that of bone is considered favorable in maximizing load sharing between the two, and thus stimulating bone formation [8–10]. However simply achieving stiffness matching through material selection is not sufficient to ensure mechanical interlock and successful osseointegration, as polyetheretherketone (PEEK) spinal interbody cages have been shown to result in fibrous encapsulation despite their relatively low

---

* Corresponding author.

E-mail address: w.walsh@unsw.edu.au (W.R. Walsh).

modulus within the range of bone [11]. Thus, it is believed that through a combination of stiffness matching, surface interaction, and three-dimensional porous networks that interfacial mechanical interlock between the implant and newly formed bone is achieved. Thus, optimization of the tradeoff between initial load bearing capacity of the implant, and long-term potential for osseointegration and load sharing must be considered.

A high strength bone-implant interface is critical to successful outcomes in many clinical applications including interbody fusion, arthroplasty fixation, and bridging of large bone defects. Clinical failure can be caused by lack of initial interlock, poor bone integration or subsequent resorption due to stress shielding, often resulting in revision surgery. This is especially challenging in treatment of segmental defects, such as those of the lower extremity, where a need for a high strength and fatigue resistant implant must be balanced with the need for bone ingrowth over a long distance [12–15]. Currently, treatment of large bone defects is primarily achieved using fibular autograft or cadaver bone allografts, the latter of which have a 50% failure rate due to nonunion and collapse after at least 16 months [16,17]. Another challenge is lack of implant integration with the host bone in arthrodesis applications, leading to instability and micromotion caused by fibrous encapsulation of the implant [18,19]. Thus, achieving early osseointegration is critical in the success of fusion procedures. We recently reported the importance of topology on establishment of a stable bone-implant interface to achieve functional repair of critically sized defects of the rat femora using gyroid-sheet implants, where the amount of bone in the most proximal and distal interfaces dictated the torsional strength of the repair [12].

Better understanding of the mechanical and biomechanical tradeoffs dictated by the implant porosity must be achieved to optimize implant design. In this study, porous titanium implants with gyroid architecture were designed with porosity varied over a physiological relevant range and produced by LPBF of medical grade titanium alloy (Ti6Al4V).

Benchtop mechanical evaluation was conducted in parallel with an ovine osseointegration model to determine the tradeoff between the implant's load bearing capabilities and the biomechanics at the bone-implant interface after 4 and 12 weeks. Histological and histomorphometric evaluations were used to assess the volume and location of bone ingrowth into the porous implants in cortical and cancellous sites. The present results have implications for orthopedic implant design across numerous clinical applications.

2. Results

2.1. Scaffold design, fabrication, and benchtop mechanical performance of titanium scaffolds

Titanium implants of varying porosity for mechanical evaluation and preclinical implantation were designed with a gyroid-sheet architecture and produced via LPBF of medical grade titanium alloy (Ti6Al4V) (Fig. 1 A, B). Porosity was systematically controlled by decreasing the wall thickness of the gyroid sheet. Porosity of the printed implants evaluated by μCT revealed a decrease in as-printed porosity from the idealized CAD model of up to 4% (Table S1). This is attributed to characteristic overinflation of the geometry resulting from the powder bed fusion process, which was seen to be the greatest in the highest porosities. Surface roughness (R_a) of the implants has previously been evaluated at 7.0 μm [7], and is resultant of the powder bed fusion process, which produces a surface with partially adherent powder particles as observed in Fig. 1 C-E. When observed at higher magnification, the spherical morphology of the titanium powder is seen to create clusters, which provide a topographical texture that is favorable for bone ongrowth as discussed below [18].

The effective strength and modulus of the scaffolds decreased in a linear manner under compressive, tensile, and torsional loading with increasing porosity (Fig. 2). Strength of the scaffold increased linearly
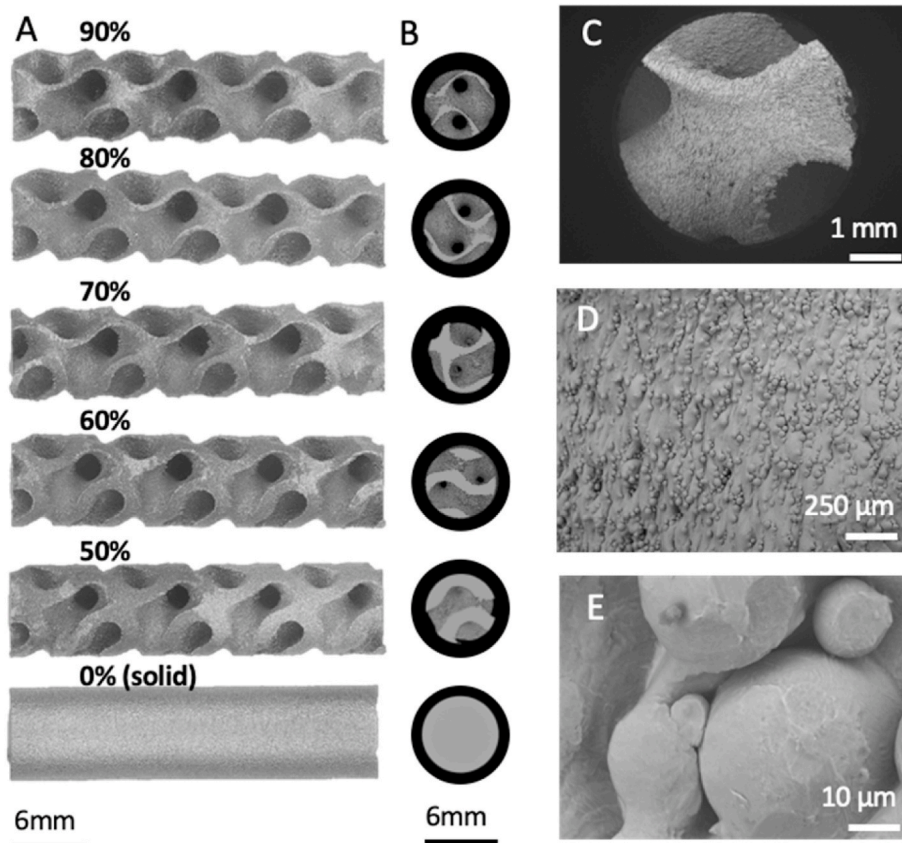
Fig. 1. Evaluation of topology and topography of titanium implants produced via laser powder bed fusion (A) Micrographs and cross-sectional images from (B) microCT reconstructions of implants with increasing porosity produced via LPBF of titanium alloy. (C–E) Micrographs of implant surface, showing the topography produced by laser powder bed fusion. At higher magnitudes, the particles are observed to create a surface topography with defined by clusters of particles forming three-dimensional features.
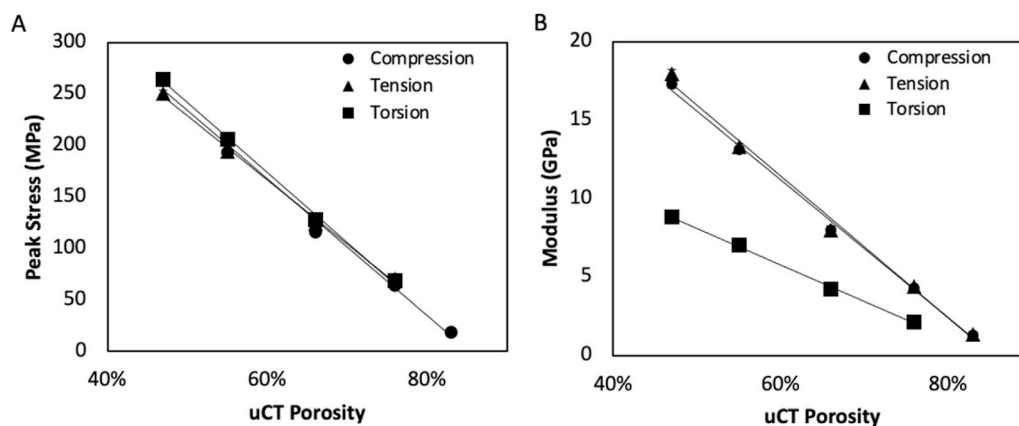
Fig. 2. Benchtop mechanical evaluation of scaffolds with increasing porosity. A linear relationship is observed with increasing porosity for scaffold **(A)** modulus and **(B)** strength under each loading mode. For all trendlines shown $R^2 > 0.99$.

ranging from 15 to 250 MPa with porosity. Across the range of porosity studied, compressive modulus varied across an order of magnitude. Shear modulus as observed to be lower than those under axial loading. This is attributed to a decrease in stiffness at the circumference of the porous gage section in torsion, particularly due to the limited number of unit cell repeats in the sample [20]. All mechanical results are tabulated in Table S1.

2.2. Evaluation of bone structure at implant surface and inside the pore network

In vivo implantation of implants with increasing porosity was conducted in a randomized manner into cancellous and cortical defect sites of adult merino sheep as shown in Fig. 3. We studied the osseointegration in cortical and cancellous sites and cortical bone-implant interface mechanical properties over a relevant implant porosity range of 50–90% by increasing the wall thickness of the gyroid-sheet and compared to a solid printed titanium implant (Fig. 1A). Histological evaluation at 4-weeks in cancellous bone sites (Fig. 4) demonstrates early new bone
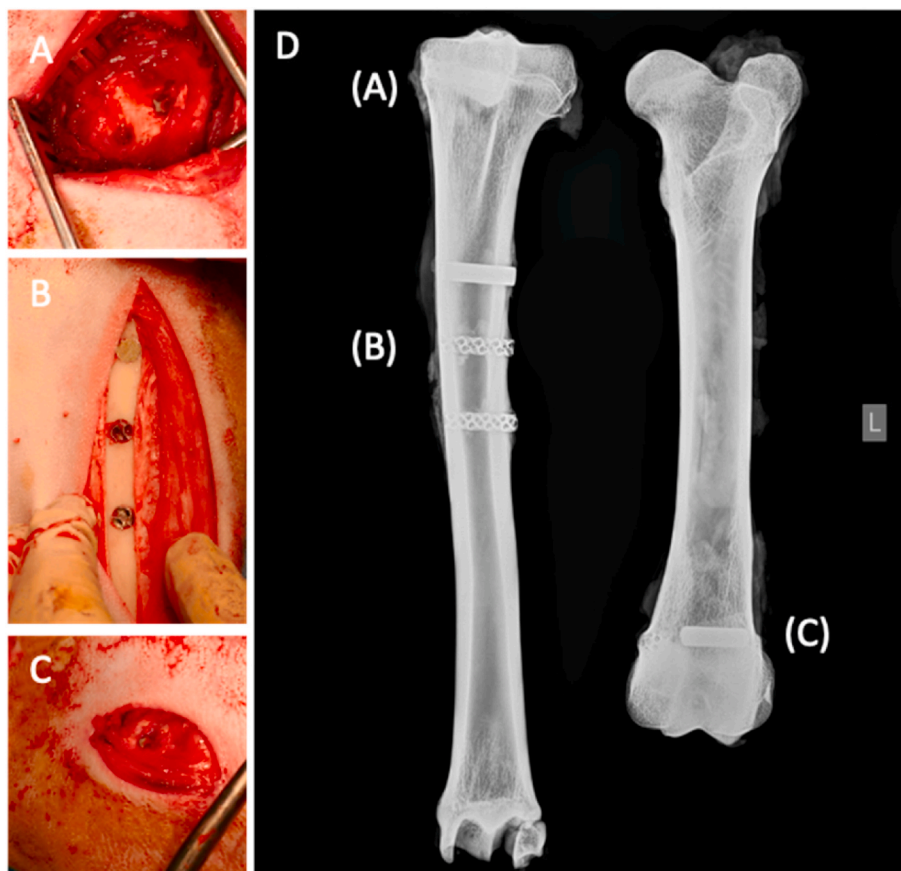
Fig. 3. Surgical implantation of titanium implants. Dowel implants were placed into one of three sites. **(A)** The proximal tibia in a press-fit manner, **(B)** the cortical bone of the diaphysis of the tibia in a line-to-line manner, **(C)** the cancellous bone of medial distal femoral condyles in a press-fit manner. **(D)** Representative ex-vivo anterior-posterior radiograph showing placement of the implants in the three sites.
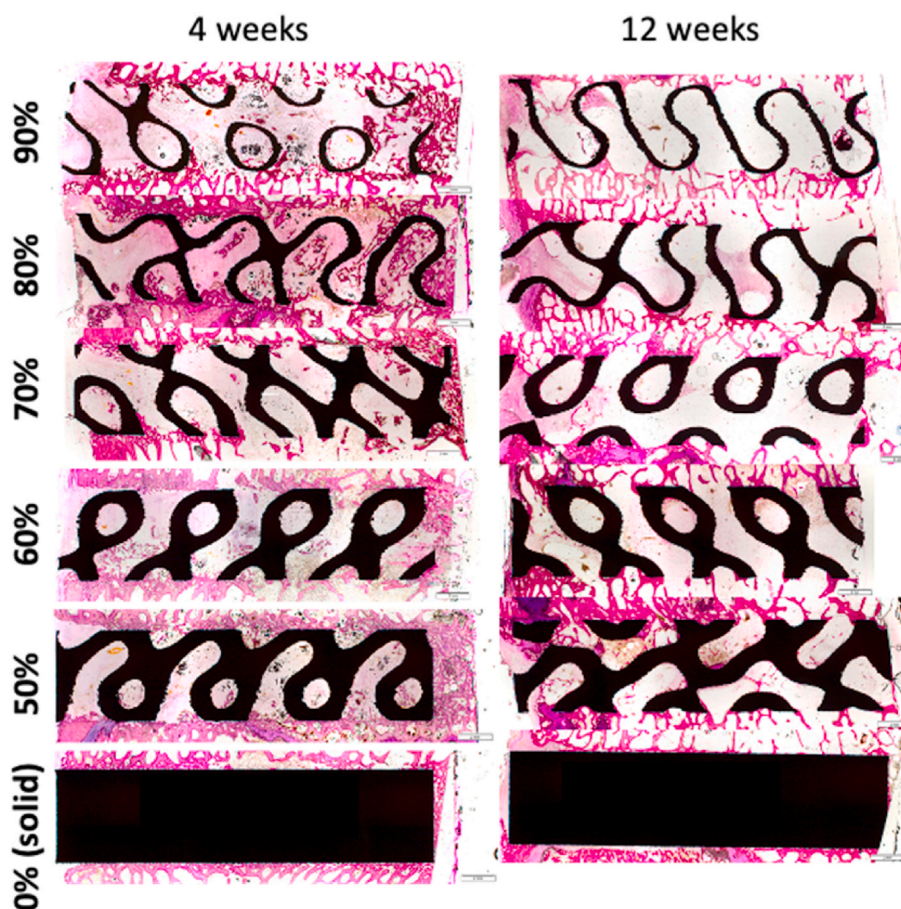
Fig. 4. Representative PMMA histology from cancellous sites at 4-weeks and 12-weeks. Limited bone ingrowth into the void space of the porous implants is observed at both time points. Most of the porous volume is filled with connective tissue in cancellous sites. Note the various geometries of the gyroid implants present in each representative image are due to location of the slice through the cross section.

deposition on the surface and integration to the titanium implant surface. By 12-weeks, limited ingrowth into the porous architecture was observed in all porous implant groups embedded in the cancellous bone, consistent with previous reports using this model in cancellous bone [21]. Conversely, in the cortical sites, early osseointegration was observed to at 4 weeks, and was seen to significantly increase by 12-weeks for all groups. Direct surface apposition to the surface topography of the implants was observed Fig. 5, and no evidence of fibrous encapsulation or inflammatory response was seen histologically in either cortical or cancellous sites.

Histomorphometry analysis of the tissues ingrown into the scaffolds in cortical sites at 4 and 12 weeks was conducted to quantify the bone ongrowth for the solid implants and ingrowth into the porous implants (Fig. 6). Tabulated histomorphometric results for solid and porous implants are given in Table S2 and Table S3 respectively. Bone Contact Length over Total Length (BCL/TL) for the solid implants in cortical sites increased from 51% to 63% at 4 and 12 weeks respectively. Bone Volume over Total Volume (BV/TV) for all porous implant groups increased from 4 to 12 weeks, as shown in Fig. 6A. To normalize for the higher void volume in higher porosity implants, Bone Volume in the Available Void (BIAV) was also calculated. At 4 weeks, the BIAV was approximately one third for all groups regardless of porosity (Fig. 6B). However, by 12 weeks, differences in bone ingrowth behavior were observed and BIAV was observed to increase with porosity, ranging from 62% for the 50% porosity implant, up to 87% BIAV for the 90% implant groups (Fig. 6B). These results indicate that bone ingrowth behavior is both temporal and porosity dependent. Specifically, at 4 weeks, woven bone deposition occurred in all groups, and was generally localized to the titanium

surface. However, by 12 weeks, the implants with more void volume available had higher *relative* ingrowth, indicating that the availability of void space facilitates neo-bone formation inside the interconnected pore network.

2.3. Implantation of porous scaffolds in sheep model to assess neo-bone formation and biomechanics

Evaluation of the biomechanics in the cortical sites after 4 and 12 weeks of implantation was conducted using a push-out test as illustrated in Fig. 7A and B. In all implant groups, the shear strength significantly increased ($p < 0.05$) from the earlier to later time point. By 4 weeks, bone ongrowth to implant surface has occurred, and by 12 weeks the deposited bone has increased in quality. This is reflected in the changes observed in the histology, histomorphometry, and pushout results from 4 to 12 week. Biomechanical results are tabulated in Table S4.

Despite higher BIAV values, high porosity implants did not exhibit higher bone-implant shear strength (Fig. 6C). The maximum force, energy to failure, and shear strength were seen to have a parabolic relationship with porosity, with a peak between 60 and 70%, the interface stiffness was seen to have an inverse linear relationship (Fig. 7C–F). At both timepoints, the 60% porosity group had the highest average shear strength (13.3 and 33.8 N/mm^2 at 4 and 12 weeks respectively). Stiffness and shear strength of the porous implants normalized to that of the solid implant at both time points are given in Fig. 7G and H respectively. A decrease in relative stiffness of the bone-implant interface from 4 to 12 weeks is seen. The relatively higher stiffness of the 50% and 60% porous implants at 4 weeks can be attributed to the greater surface area in direct
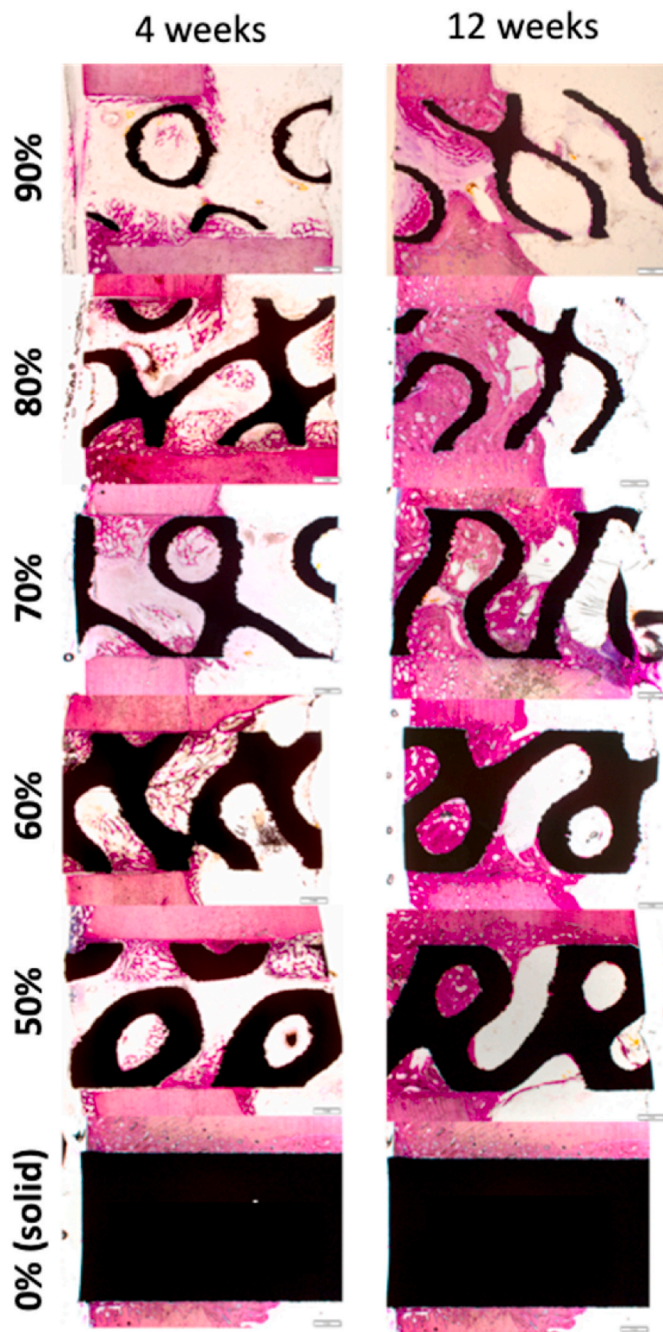
Fig. 5. Representative PMMA histology from cortical sites at 4-weeks and 12-weeks. Progressive bone ingrowth into the void space of the porous implants is observed from early the mid time points. At 4-weeks At 12-weeks the porous volume of most of the porous implants were filled with newly formed bone. Note the various geometries of the gyroid implants present in each representative image are due to location of the slice through the cross section.

apposition to the cortex, allowing early fixation involved at the interface. By 12 weeks, despite the increased bone volume observed in the higher porosity implants, increased shear strength as not observed. Bone located in the center of the porous implants does not contribute to shear resistance, thus the shear strength is dependent on the amount and maturity of the bone at the cortical interface.
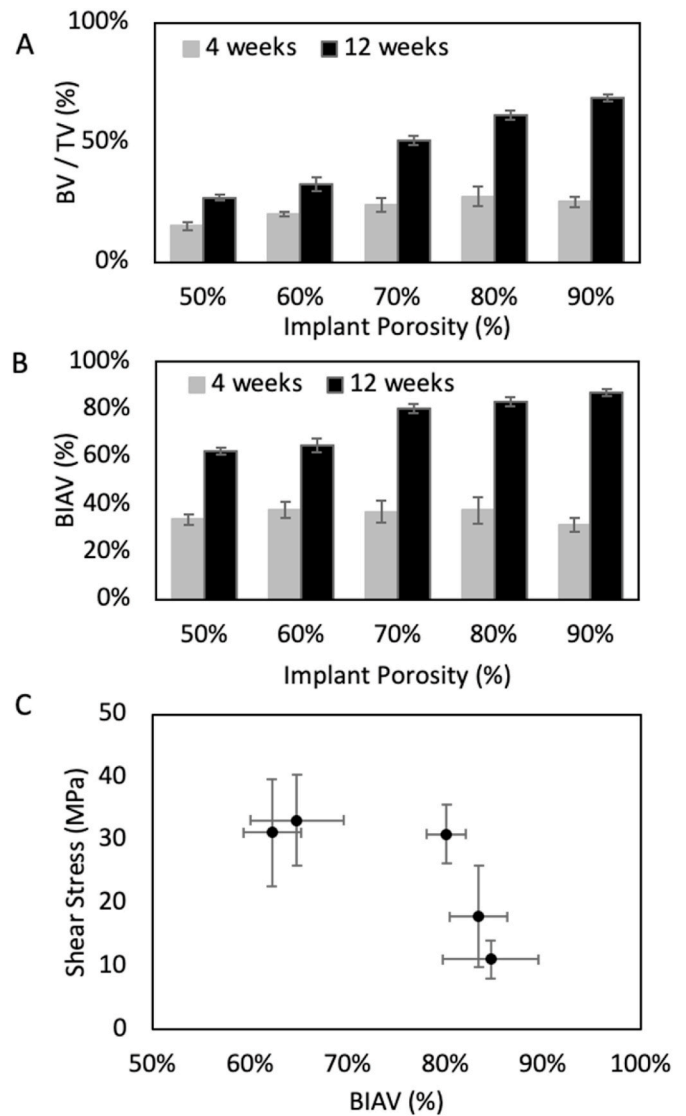

Fig. 6. Bone ingrowth increases with increasing porosity. (A) Bone volume (BV) assessed via histomorphometry for implants with increasing porosity. (B) Normalization of BV by the void volume is represented by bone in the available void (BIAV). (C) An indirect relationship is observed between BIAV versus shear strength assessed at 12-weeks.

2.4. Limb salvage in patients with critical sized defects of the lower extremities

Early clinical evidence for use of anatomically matched porous titanium implants produced by LPBF indicate a significant improvement upon previous reconstructive options using bulk allograft [14,15,21,22]. However, reconstructive failure due to implant fracture and inability to achieve implant integration have been reported and is increased in patients with comorbidities such as diabetes, smoking, or history of infection [14,15].

Two representative case reports demonstrating successful outcomes after treatment with patient-specific implants with gyroid lattice for reconstruction of large segmental defects of the tibia and femur are shown here. In both cases, postoperative radiographic results have shown bone formation in and around the implant surface. In the case of the 21-year-old female who sustained an open fracture of the distal tibia with substantial bone loss, bone growth is observed radiographically as early as 4 months along the posterior side of the implant (Fig. S1). In the case of the 60-year-old male treated for fracture of the distal femur, bone
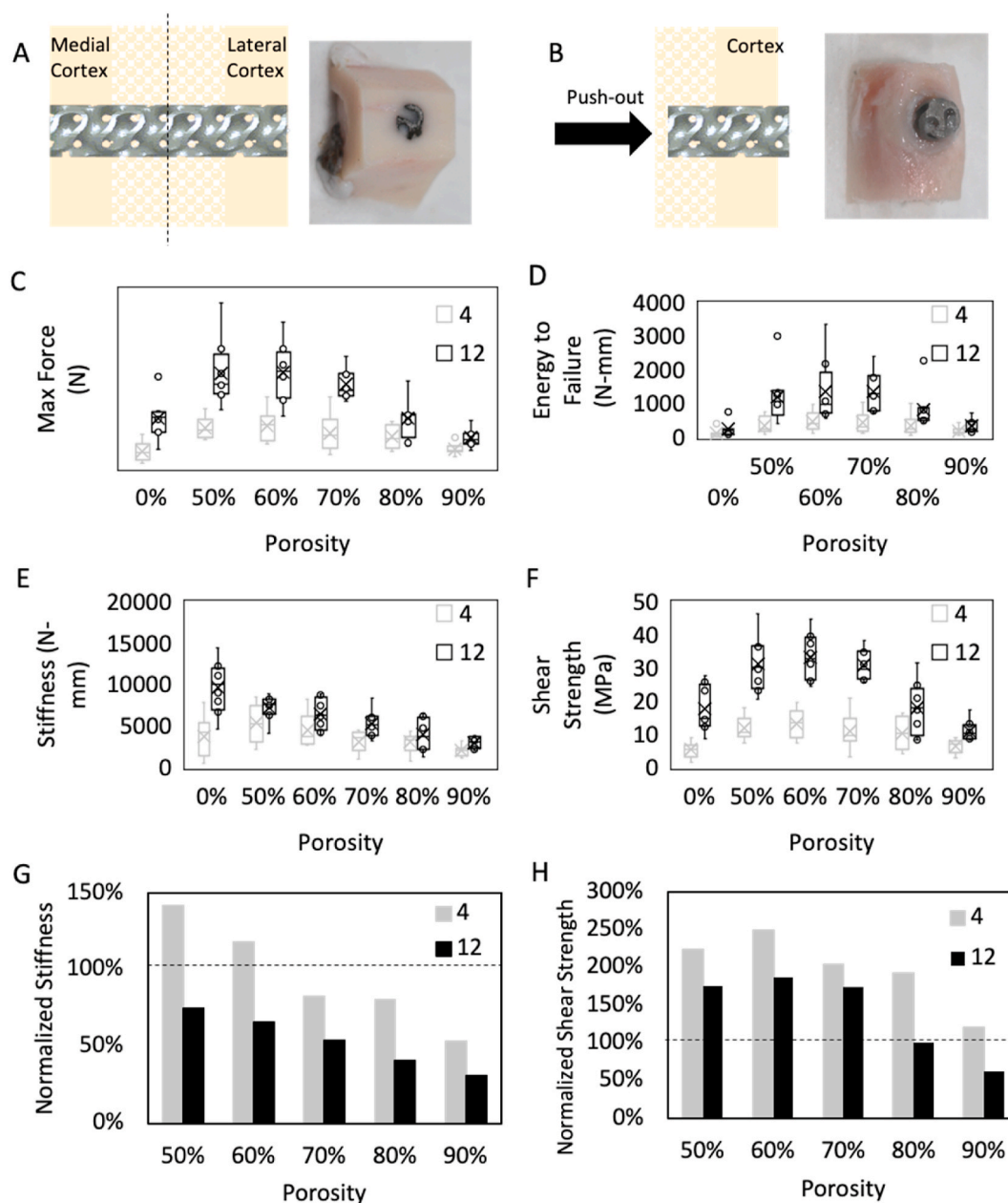
Fig. 7. Biomechanical evaluation via push-out test performed at 4 and 12 weeks after implantation. (A, B) Schematic and images of sectioning and push-out of implant from cortex. **(C–F)** Push-out results given at 4 weeks (grey) and 12 weeks (black). Max force, energy to failure, stiffness, and shear strength. Biomechanical results for implants with increasing porosity normalized by that of the solid implants at the same time point; **(G)** Normalized stiffness, **(H)** Normalized shear stress.

formation along the surface of the implant is observed radiographically at 12 months (Fig. S2). Given the radiodensity of the titanium implants, quantification of bone ingrowth into the porous network of the implants was not possible using X-ray or CT imaging because of the inability to distinguish bone formation from metal artifact.

3. Discussion

The present mechanical, preclinical, and clinical results establish the use of porous titanium implants with gyroid-sheet architecture produced by AM for treatment of load-bearing bone defects and overall implant fixation. Driven by recent evidence that the role of substrate curvature is important in cuing tissue regeneration [23], gyroid and other TPMS-based architectures have received greatly increased interest for use as tissue engineering scaffolds as they have been shown to have local curvature and stiffness similar to human bone [3,6,24–27]. Gyroid-sheet

topologies are hypothesized to enable enhanced bone ingrowth due to the high surface area, permeability, capacity to effectively carry biologics, and potential for the sheet curvature to drive osteogenic cues. We hypothesized that with increasing porosity, a reduction in modulus would be observed, and result in improved osseointegration performance due to increased void volume for bone ingrowth. The results of the current study agree with previous reports using the same ovine model [28–30] and allows for the first time an understanding or the influence of porosity volume fraction on mechanical properties and in vivo performance in a controlled manner.

Porous scaffolds can be thought of as composites, where the topological distribution of the material in a void matrix gives varied properties at the macroscale [3,21,28,31–33]. For bone scaffolds, this means modulation of strength and stiffness, by controlling the porosity and architecture. Evaluation of porous architectures such as the gyroid-sheet under torsional and compressive loading is pertinent to its use in

orthopedic implants. Although compressive loads are the dominant physiological loading mode, bending and torsional loads are also observed [12,34]. The gyroid-sheet architecture evaluated has previously been shown to have high strength and stiffness relative to other porous architectures, for example compared to an octet truss of the same porosity [3,6,20,35,36]. The superior compressive strength and energy absorption is attributed to the continuous nature of the sheets, which serves to more homogeneously distribute load [37]. Further, the sheets are self-supporting during the printing process, which results in fewer geometric imperfections that can drive enhanced local stress concentrations [3], or that may act as notched stress concentrations leading to early fatigue failure [4,6].

The moduli and strength of the gyroid-sheet scaffolds under both loading modes was seen to be similar and within the range of cancellous and cortical bone [38]. The dependence on porosity was greater than on loading mode, supporting previous studies showing the relative isotropic nature of the gyroid architecture [39]. Compressive strength ranged over an order of magnitude (30–300 MPa) depending on porosity, indicating there is a wide design window for topological optimization of an implant dependent on loading criteria for various orthopedic applications. Both compressive strength and moduli were reduced from previously reported properties of gyroid-sheet scaffolds, which is attributed to the influence of free boundary effects which reduce the properties of porous scaffolds when the number of unit cell repeats is low, as it was in this study [20].

Early bone formation at in both the cancellous and cortical sites was mediated by the titanium implant's osteoconductive surface. Direct apposition on bone to the rough surface of the implant indicates the roughness resulting from LPBF is appropriate for facilitating attachment via ongrowth. Previous results from other osteointegration preclinical studies have also shown the influence of topography of rough surfaces resulting from PBF of titanium implants [18,19]. The 4-week shear strength of gyroid-sheet implants is greater than previously reported values for porous implants with diamond grid architecture using the same model [28]. This is attributed to the higher surface area of the

gyroid which is advantageous for maximizing bone contact for early stabilization. At the later time point, bone formation patterns appeared to be guided by the curvature of the implant topology. Given the sinusoidal nature of the gyroid architecture, which has both convex and concave surfaces, bone ingrowth into the center of the implant was facilitated. Recent evidence surrounding topology driven bone growth, and particularly the role of substrate curvature further supports the design of present implants with gyroid-sheet architecture [31,40].

The remodeling of bone at later time points is dependent on the interface mechanics which are themselves dependent on the topology of the implant, dictated by the structure and porosity. The tradeoff between osseointegration, as evaluated by shear strength, and the initial load bearing capacity, as measured by compressive strength, is not direct (Fig. 8A). Thus, based on this work, a mechanically and biomechanically balanced implant can be designed based on the necessary orthopedic application. However, a limitation of the present study is the uncertainty of the in vivo performance at longer endpoints where more significant bone remodeling may occur. Given longer implantation periods, higher porosity scaffolds may indeed reach shear strengths equivalent to lower porosity implant and provide for improved load sharing. Further, evaluation of bone remodeling in the adjacent cortex inferior and superior to the defect sites, as well as within the implants at later timepoints would be valuable for understanding the role of implant stiffness on long-term biomechanics.

The roles of both surface topography and porous topology are important in achieving osseointegration of implants. Present gyroid implants were observed to have higher shear strength at 12 weeks than previously reported values for smooth titanium, as well as plasma spray coated, or grit blasted + HA coated surface (Fig. 8B) [41,42]. Non-additive manufacturing methods such as plasma spray or HA coating enable rough surfaces or deposition of mineralized coating towards improve bone-implant interface strength. However, these processes require additional manufacturing steps to deposit the surface coating, which are typically limited by line-of-sight deposition, and vulnerable to delamination from the substrate. Conversely, one of the
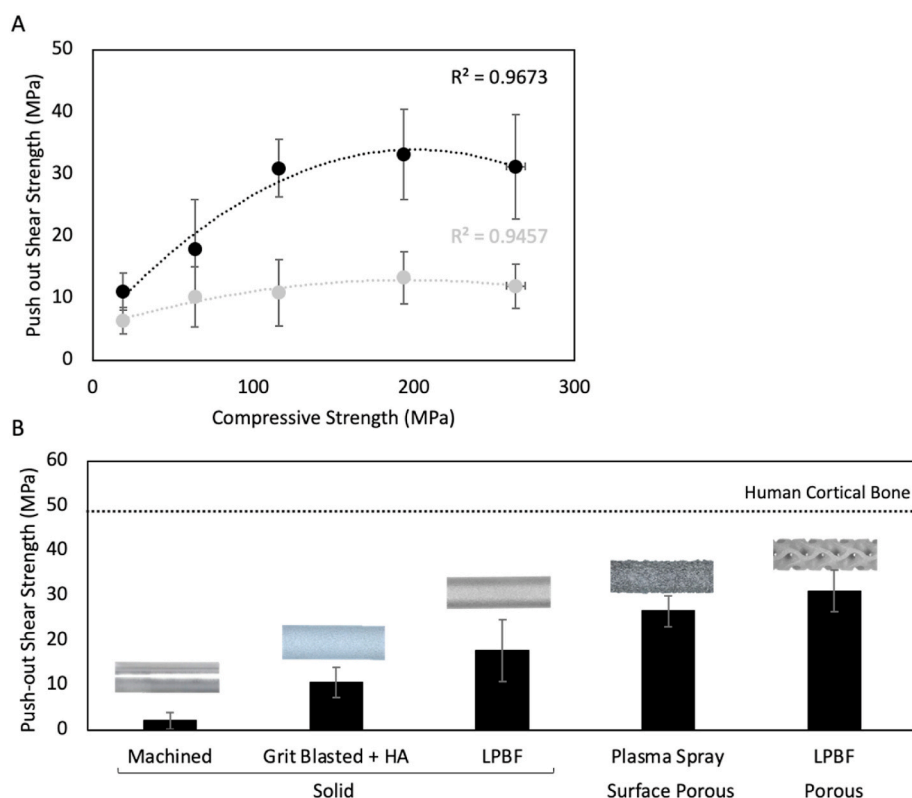
Fig. 8. Bone-implant interface biomechanics are driven by topography and topology, both of which are highly tunable using 3D Printing Technology. (A) Shear strength at 4 and 12 weeks versus compressive strength of empty scaffold. (B) Shear strength of solid titanium implants with varied surface roughness, compared with surface porous, and porous 3D printed implants evaluated at 12-weeks in an ovine bone defect model. 3D Printing enables "complexity for free" including the ability to manufacture implants with high surface roughness and complex porous architectures to optimize mechanical interlock to bone [21,52].

hallmark advantages of AM technologies is "complexity for free", meaning design of surface topography and porous topology are inherent to the manufacturing. Given this advantage, use of LPBF to manufacture porous implants for hip, knee, spine, and foot and ankle indications has been increasingly adopted [1].

In a recent case series reporting outcomes from complex reconstructions of the foot and ankle using AM titanium implants in high-risk patients, 87% were successful, however the failures were due to non-union (6%) and infection (6%) [14]. Although there are some preliminary preclinical results [12,43], further work in evaluation of the efficacy of such high strength porous implant to support load bearing while acting as a carrier for delivery of osteoinductive or antibiotic materials would be highly valuable in translation to the clinic. In the reconstructive case shown in Fig. S2, for example, the patient was previously treated for an infection due to the open fracture prior to placement of the porous titanium implant. While the implants in this preclinical study were not packed with biologics, however in clinical use porous titanium implants are typically packed with autogenic, allogenic, or synthetic bone graft to promote bony fusion [28,44–48]. Similarly, treatment of infections with localized antibiotics could be facilitated through such composited implants, which could be an avenue for future work in this area. Additionally, a growing area of research is investigation of degradable metallics, including Mg, Zn, and Fe, produced by LPBF for orthopedic applications [49–51]. These materials may offer an advantage to titanium scaffolds, as they can degrade over time and be replaced by newly forming bone.

4. Conclusion

In this work, demonstration of a linear relationship between scaffold porosity and mechanical performance was observed, whereas a parabolic relationship with ex vivo pushout strength was seen. All porosities showed an increase in pushout shear strength from the 4 week–12 week timepoint. The highest pushout strength of the porous titanium gyroid implants at both the time points evaluated in a bicortical defect model was 60% porosity implants, which exceeded previously reported values for titanium implants with plasma spray coated or other modified surfaces previous reported in this preclinical model. These results show that while an increase in mechanical interlock strength through osseointegration can be achieved with porous scaffolds, there is diminishing return in both strength and bone ingrowth in scaffolds with porosity exceeding 80%.

5. Materials and methods

5.1. Study design

The objectives of the study were to establish a relationship between mechanical and biological performance of porous titanium scaffolds produced by AM for use in treatment of bone defects using patient-specific implants. Laser powder bed fusion (LPBF) of medical grade titanium alloy was used to manufacture implants with increasing porosity which were evaluated in a bicortical defect model in sheep. Bone-implant interface biomechanics were assessed, along with histological evaluation at 4 and 12 weeks. Analogous porous specimens were produced for benchtop mechanical evaluation under tensile, torsional, and compressive loading to determine each's modulus and strength.

5.2. Design and manufacturing

As described above, the gyroid sheet architecture is defined by sinusoidal functions which can be used to generate a unit cell that can be patterned to fill a defined geometric volume. The present coupons and implants were designed based on a repeating gyroid-sheet cubic unit cell, with side length of 6 mm. The porosity of the scaffolds was modulated by increasing the wall thickness of the sheets, such that with increasing thickness, the porosity of the resulting scaffold decreased, as shown in S.I. Table 1. Additionally, solid coupons and implants with no porosity were designed as a control. Coupons and implants were fabricated via LPBF according to ASTM F3001. LPBF was conducted on a 3D Systems ProX DMP 320, using Ti6Al4V ELI powder under inert argon atmosphere. Printing parameters followed previously reported methods optimized for gyroid lattices [4]. Following printing, excess powder was cleaned from all samples, which then underwent hot isostatic pressing (in accordance with ASTM F3001, $900°C$ at 1000 bar for 2 h) prior to removal from the build plate by wire electrical discharge machining. A surface blasting treatment which removes any partially adhered powder, followed by passivation in nitric acid, and cleaning was conducted on all coupons and implants. Implants were then sterilized via gamma irradiation prior to surgery. In LBPF, and other additive manufacturing technologies, deviation of the printed part from the idealized CAD model is common, particularly when there are features close to the resolution of the printing method or unsupported geometries. Micro-computed tomography (μCT) was used to compare the porosity of the printed implant to that of the designed CAD model.

5.3. Mechanical evaluation

Representative coupons of the solid and various gyroid-sheet porosities were tested under compressive, tensile, and torsional loading. All mechanical testing was conducted on a calibrated servo-electric testing frame (Test Resources 830, 50 kN load cell) under displacement control. Compressive and tensile loads were applied at an axial displacement rate of 1 mm/min, and torsional tests were conducted at a rate of 1°/second. All tests were conducted until sample failure. For each loading mode, peak stress, yield stress, and modulus were calculated from the stress-strain curves, using and the total cross-sectional area of the sample to calculate stress. The highest porosity (90%) specimens for tensile and torsion testing were too fragile for mechanical testing, and thus no results are reported.

5.4. Ovine bicortical defect model

Following institutional ethical approval (UNSW ACEC 20/36A) an established ovine bone ingrowth/ongrowth model and endpoints that have been reported for over two decades with various technologies for osseointegration [21,29,47,52–60] was used for the in-vivo portion of the study. Sample size (n = 5) was based on a power calculation to detect a 20% difference between groups. Ten skeletally mature adult male sheep (Border Leicester Merino Cross, Ovis Aries, 18 months) underwent a bilateral procedure with implants placed in a press fit manner (5.5 mm hole and 6 mm implant) into the cancellous bone of the distal femur (2 implants per femur) and proximal tibias (1 implant per tibia) well as bicortical diaphysis of the tibia (3 implants per tibia) in a line-to-line manner (6 mm hole and 6 mm implant) (Fig. 3). The model provided a total of 6 cancellous and 6 cortical sites per animal.

Pre-operative animal preparation included a clinical veterinary review as well as routine haematology and biochemistry blood work to confirm animal status. Fentanyl patches (2–3 μg/kg/hr) (company name here) were used to provide an opioid analgesic 24 h prior to surgery [61]. The animals were sedated with xylazine Intramuscular injection, (IM)) followed by ketamine (IM) 15 min later. The animals were intubated and maintained throughout the procedure on oxygen and isoflurane using an anesthetic machine. All animals received 1 g of Cefazolin intravenously and Benacillin (Procaine penicillin) 1mL/10 kg (IM) after induction as antibiotic prophylaxis as well as IV Hartmann's fluid during the procedure via an 18-gauge cannula placed in the cephalic vein. The fentanyl patches were replaced to provide analgesia cover for approximately 72 h ([61].

The skin on the medial aspect of tibias and femurs were clipped and aseptically prepared for surgery with chlorhexidine gluconate 4% w/v in ethanol (96%) and allowed to dry. The animals were transferred to the

operating theatre and placed on the surgical table and positioned supine. A final spray of 70% providone iodine was applied all over the clipped surgical site and draped for surgery. The cancellous or cortical bone sites were exposed, and a hole created using a 4.5 mm drill bit for a pilot hole followed by 5.5 mm drill bit in cancellous bone to allow a press fit or a 6 mm drill bit in cortical bone for a line to line fit. Saline hydration was used to minimize any thermal damage during drilling. Six different implants (table x) were randomly allocated cortical and cancellous sites. The subcutaneous and skin were closed in layers using resorbable sutures. Post-operative pain relief was provided by the fentanyl patch as well as Carprofen (Rimadyl) for the first 48 h (subcutaneous injection). Animals were carefully monitored throughout the study. Five animals were euthanized and 4- and 12-weeks after surgery for the endpoints as outlined below and reported in previous work [21,29,47,52–60].

On the day of euthanasia, general health status, ambulation and blood work was repeated along with the sedation and anesthetic procedure described above prior to lethal injection with an overdose sodium pentobarbitone (Lethobarb) via the jugular vein. The right and left skin and subcutaneous sites were inspected for any sign of wound breakdown or infection. The femur and tibia were harvested intact and radiographed in the antero-posterior and lateral planes using a Faxitron (Faxitron, Wheeling, IL) and digital plates (AGFA CR MD4.0 Cassette). Radiographs in the anteroposterior and lateral views were carefully examined to assess for any adverse bony reactions, and evidence of radiographic changes at the implant bone interface.

The implants placed in the cancellous bone were isolated with a saw, fixed in cold phosphate-buffered formalin and processing using routine polymethylmethacrylate (PMMA) embedding. The bicortical implants in the tibia were isolated using a saw in the axial plane and sectioned in the sagittal plane to isolate the medial and lateral specimens for push-out testing followed by PMMA hard-tissue histology. Prior to mechanical testing, the specimens were polished using a Buehler polisher perpendicular to the long axis of the implant to remove any periosteal bone overgrowth.

A calibrated servohydraulic testing machine (MTS Mini Bionix, MTS Systems Inc., Minneapolis, MN, USA) was used with a 25 kN load cell to perform a standard pushout test of the implants in cortical bone at 0.5 mm/min until the peak load was reached. All samples were fixed in phosphate buffered formalin and processed for routine PMMA histology. Peak load, stiffness, and energy to failure were determined by plotting of the load-deformation curve and calculated using a MATLAB script (MATLAB R2016a, MathWorks, Natick, MA, USA). The shear stress (Eq. (1)) where σ is the shear stress, c1 and c2 are the cortical thickness on each side of the implant in the histology section, and d is the implant diameter. After obtaining cortical thickness values from the PMMA histology.

$$\sigma = \frac{Load}{\left(\frac{c_1 + c_2}{2}\right)\pi d_i}$$ (Equation 1)

Histology processing included phosphate buffered formalin fixation followed by dehydration in increasing concentrations of ethanol followed by methylmethacrylate and polymerization. Embedded cortical and cancellous samples were sectioned along the long axis of the implants using a Leica SP 1600 Microtome (Leica Biosystems, Nussloch, Germany). A minimum of two thin ($\sim$15–20 μm) sections were cut from sample, etched in acidic ethanol (98 mL ethanol 96% and 2 mL HCl 37%) and stained with methylene blue followed by basic fuchsin.

The stained slides were reviewed under low magnification to provide an overview of the section and histomorphometry for bone ingrowth and ongrowth. The implant-bone interfaces and local reactions were carefully examined at higher magnification for the presence of inflammatory cells or local particulate in the cancellous and cortical sites as well as the bone reaction on as well as withing the porous domains of the gyroid. Histology images were used for bone ingrowth and ongrowth histomorphometry using validated internal programs (MatLab scripts) to assess the amount of bone ingrowth as well as implant material in each section.

5.5. Statistical methods

Mechanical data is presented as the average and standard deviation. Histomorphometry data was analyzed by determining a single mean value for each implant site from the multiple sections and pooled for each group in cortical or cancellous sites for statistical analysis using a two-way ANOVA and post-hoc multiple comparisons with $p < 0.05$ chosen for significant using SPSS (IBM Ver 25). The pushout biomechanical results are presented as average and standard error. A two-way ANOVA and post-hoc multiple comparisons test with $p < 0.05$ was used to assess the pushout results.

Declaration of competing interest

The authors declare the following financial interests/personal relationships which may be considered as potential competing interests: Cambre Kelly reports a relationship with restor3d, Inc. that includes: equity or stocks. Ken Gall reports a relationship with restor3d, Inc. that includes: equity or stocks. Samuel B. Adams reports a relationship with restor3d, Inc. that includes: equity or stocks.

Acknowledgments

Appendix A. Supplementary data

Supplementary data to this article can be found online at https://doi.org/10.1016/j.biomaterials.2021.121206.

Funding

Author contributions

Conceptualization: CK, KG, WRW. Investigation: CK, TW, MHP, DW, JC, WRW. Writing – original draft: CK, WRW. Writing – review & editing: CK, TW, MHP, DW, JC, TW, KG, WRW.

Data and materials availability

All data are available in the main text or the supplementary materials.

References

[1] L.M. Ricles, J.C. Coburn, M. Di Prima, S.S. Oh, Regulating 3D-printed medical products, Sci. Transl. Med. 10 (2018).
[2] C.N. Kelly, A.T. Miller, S.J. Hollister, R.E. Guldberg, K. Gall, Design and structure–function characterization of 3D printed synthetic porous biomaterials for tissue engineering, Adv. Healthcare Mater. 7 (2018) 1701095.
[3] O. Al-Ketan, R. Rowshan, R.K. Abu Al-Rub, Topology-mechanical property relationship of 3D printed strut, skeletal, and sheet based periodic metallic cellular materials, Addit. Manuf. 19 (2018) 167–183.
[4] C.N. Kelly, et al., Fatigue behavior of as-built selective laser melted titanium scaffolds with sheet-based gyroid microarchitecture for bone tissue engineering, Acta Biomater. 94 (2019) 610–626.
[5] O. Al-Ketan, R.K. Abu Al-Rub, Multifunctional mechanical metamaterials based on triply periodic minimal surface lattices, Adv. Eng. Mater. 21 (2019).
[6] F.S.L. Bobbert, et al., Additively manufactured metallic porous biomaterials based on minimal surfaces: a unique combination of topological, mechanical, and mass transport properties, Acta Biomater. 53 (2017) 572–584.
[7] C.N. Kelly, et al., The effect of surface topography and porosity on the tensile fatigue of 3D printed Ti-6Al-4V fabricated by selective laser melting, Mater. Sci. Eng. C 98 (2019) 726–736.

[8] J.H. Chen, C. Liu, L. You, C.A. Simmons, Boning up on Wolff's Law: mechanical regulation of the cells that make and maintain bone, J. Biomech. 43 (2010) 108–118.

[9] H.M. Frost, Wolff's Law and bone's structural adaptations to mechanical usage: an overview for clinicians, Angle Orthod. 64 (1994) 175–188.

[10] J.C. Rice, S.C. Cowin, J.A. Bowman, On the dependence of the elasticity and strength of cancellous bone on apparent density, J. Biomech. 21 (1988) 155–168.

[11] W.R. Walsh, N. Bertollo, C. Christou, D. Schaffner, R.J. Mobbs, Plasma-sprayed titanium coating to polyetheretherketone improves the bone-implant interface, Spine J. 15 (2015) 1041–1049.

[12] C.N. Kelly, et al., Functional repair of critically sized femoral defects treated with bioinspired titanium gyroid-sheet scaffolds, J. Mech. Behav. Biomed. Mater. 116 (2021).

[13] J.C. Reichert, et al., The challenge of establishing preclinical models for segmental bone defect research, Biomaterials 30 (2009) 2149–2163.

[14] T.J. Dekker, J.R. Steele, A.E. Federer, K.S. Hamid, S.B. Adams Jr., Use of patient-specific 3D-printed titanium implants for complex foot and ankle limb salvage, deformity correction, and arthrodesis procedures, Foot Ankle Int. 39 (8) (2018) 916–921, 1071100718770133.

[15] K.S. Hamid, S.G. Parekh, S.B. Adams, Salvage of severe foot and ankle trauma with a 3D printed scaffold, Foot Ankle Int. 37 (2016) 433–439.

[16] C.L. Jeng, J.T. Campbell, E.Y. Tang, R.A. Cerrato, M.S. Myerson, Tibiotalocalcaneal arthrodesis with bulk femoral head allograft for salvage of large defects in the ankle, Foot Ankle Int. 34 (2013) 1256–1266.

[17] W. Wang, K.W.K. Yeung, Bone grafts and biomaterials substitutes for bone defect repair: a review, Bioact Mater 2 (2017) 224–247.

[18] A. Cheng, et al., Laser sintered porous Ti-6Al-4V implants stimulate vertical bone growth, Ann. Biomed. Eng. 45 (2017) 2025–2035.

[19] A. Cheng, A. Humayun, D.J. Cohen, B.D. Boyan, Z. Schwartz, Additively manufactured 3D porous Ti-6Al-4V constructs mimic trabecular bone structure and regulate osteoblast proliferation, differentiation and local factor production in a porosity and surface roughness dependent manner, Biofabrication 6 (2014), 045007.

[20] A. Pham, C. Kelly, K. Gall, Free boundary effects and representative volume elements in 3D printed Ti–6Al–4V gyroid structures, J. Mater. Res. (2020) 1–9.

[21] W.R. Walsh, et al., Does implantation site influence bone ingrowth into 3D-printed porous implants? Spine J. 11 (2019) 1885–1898.

[22] S.C. Anne-Marie Pobloth, Hajar Razi, Ansgar Petersen, James C. Weaver, Katharina Schmidt-Bleek, Markus Windolf, Andras Á. Tatai, Claudia P. Roth, Klaus-Dieter Schaser, Georg N. Duda, Philipp Schwabe, Mechanobiologically optimized 3D titanium-mesh scaffolds enhance bone regeneration in critical segmental defects in sheep, Sci. Transl. Med. 10 (2018) 423.

[23] S.J.P. Callens, R.J.C. Uyttendaele, L.E. Fratila-Apachitei, A.A. Zadpoor, Substrate curvature as a cue to guide spatiotemporal cell and tissue organization, Biomaterials 232 (2019) 119739.

[24] J. Shi, et al., A TPMS-based method for modeling porous scaffolds for bionic bone tissue engineering, Sci. Rep. 8 (2018) 7395.

[25] D. Mahmoud, M.A. Elbestawi, Selective laser melting of porosity graded lattice structures for bone implants, Int. J. Adv. Manuf. Technol. 100 (2018) 2915–2927.

[26] S. Vijayavenkataraman, L. Zhang, S. Zhang, J.Y.H. Fuh, W.F. Lu, Triply periodic minimal surfaces sheet scaffolds for tissue engineering applications: an optimization approach towards biomimetic scaffold design, ACS Appl. Bio Mater. 1 (2) (2018) 259–269.

[27] O. Al-Ketan, D.W. Lee, R. Rowshan, R.K. Abu Al-Rub, Functionally graded and multi-morphology sheet TPMS lattices: design, manufacturing, and mechanical properties, J. Mech. Behav. Biomed. Mater. 102 (2019) 103520.

[28] W.R. Walsh, et al., Does implantation site influence bone ingrowth into 3D-printed porous implants? Spine J. 19 (11) (2019) 1885–1898.

[29] N. Bertollo, E. Sandrini, P.D. Pria, W.R. Walsh, Osseointegration of multiphase Anodic spark deposition treated porous titanium implants in an ovine model, J. Arthroplasty 30 (2015) 484–488.

[30] M. Svehla, P. Morberg, W. Bruce, B. Zicat, W.R. Walsh, The effect of substrate roughness and hydroxyapatite coating thickness on implant shear strength, J. Arthroplasty 17 (2002) 304–311.

[31] A.A. Zadpoor, Bone tissue regeneration: the role of scaffold geometry, Biomater. Sci. 3 (2015) 231–245.

[32] W.R. Walsh, et al., Does implantation site influence bone ingrowth into 3D-printed porous implants? Spine J. 19 (2019) 1885–1898.

[33] A.A. Zadpoor, Mechanical performance of additively manufactured meta-biomaterials, Acta Biomater. 85 (2018) 41–59.

[34] J. van der Stok, et al., Enhanced bone regeneration of cortical segmental bone defects using porous titanium scaffolds incorporated with colloidal gelatin gels for time- and dose-controlled delivery of dual growth factors, Tissue Eng. 19 (2013) 2605–2614.

[35] L. Zhang, et al., Energy absorption characteristics of metallic triply periodic minimal surface sheet structures under compressive loading, Addit. Manuf. 23 (2018) 505–515.

[36] I. Maskery, N.T. Aboulkhair, A.O. Aremu, C.J. Tuck, I.A. Ashcroft, Compressive failure modes and energy absorption in additively manufactured double gyroid lattices, Addit. Manuf. 16 (2017) 24–29.

[37] E. Gawronska, R. Dyja, N. Sczygiol, Numerical simulations of stress distribution in complex structures with various average volume fraction, Proceed. World Congr. Eng. Comput. Sci. II (2018).

[38] W.R. Walsh, N. Guzelsu, Compressive properties of cortical bone: mineral-organic interfacial bonding, Biomaterials 15 (1994) 137–145.

[39] H. Barber, C.N. Kelly, K. Nelson, K. Gall, Compressive anisotropy of sheet and strut based porous Ti–6Al–4V scaffolds, J. Mech. Behav. Biomed. Mater. 115 (2021) 104243.

[40] A.A. Zadpoor, Mechanics of additively manufactured biomaterials, J. Mech. Behav. Biomed. Mater. 70 (2017) 1–6.

[41] M. Svehla, et al., Morphometric and mechanical evaluation of titanium implant integration: comparison of five surface structures, J. Biomed. Mater. Res. 51 (2000) 15–22.

[42] W.R. Walsh, et al., Bone ongrowth and mechanical fixation of implants in cortical and cancellous bone, J. Orthop. Surg. Res. 15 (2020) 177.

[43] J. van der Stok, et al., Full regeneration of segmental bone defects using porous titanium implants loaded with BMP-2 containing fibrin gels, Eur. Cell. Mater. 29 (2015) 141–153, discussion 153-144.

[44] H. Yuan, et al., Osteoinductive ceramics as a synthetic alternative to autologous bone grafting, Proc. Natl. Acad. Sci. U. S. A 107 (2010) 13614–13619.

[45] P. Habibovic, K. de Groot, Osteoinductive biomaterials–properties and relevance in bone repair, J Tissue Eng Regen Med 1 (2007) 25–32.

[46] R. Dimitriou, E. Jones, D. McGonagle, P.V. Giannoudis, Bone regeneration: current concepts and future directions, BMC Med. 9 (2011) 66.

[47] D. Chen, et al., Osseointegration of porous titanium implants with and without electrochemically deposited DCPD coating in an ovine model, J. Orthop. Surg. Res. 6 (2011) 56.

[48] L. Mullen, R.C. Stamp, W.K. Brooks, E. Jones, C.J. Sutcliffe, Selective Laser Melting: a regular unit cell approach for the manufacture of porous, titanium, bone in-growth constructs, suitable for orthopedic applications, J. Biomed. Mater. Res. B Appl. Biomater. 89 (2009) 325–334.

[49] Y. Li, et al., Additively manufactured biodegradable porous iron, Acta Biomater. 77 (2018) 380–393.

[50] Y. Qin, et al., Additive manufacturing of biodegradable metals: current research status and future perspectives, Acta Biomater. 98 (2019) 3–22.

[51] Y. Yang, et al., In-situ deposition of apatite layer to protect Mg-based composite fabricated via laser additive manufacturing, J. Magn. Alloys (2021), https://doi.org/10.1016/j.jma.2021.04.009.

[52] M. Svehla, et al., Morphometric and mechanical evaluation of titanium implant integration: comparison of five surface structures, J. Biomed. Mater. Res. 51 (2000) 15–22.

[53] M. Svehla, P. Morberg, W. Bruce, B. Zicat, W.R. Walsh, The effect of substrate roughness and hydroxyapatite coating thickness on implant shear strength, J. Arthroplasty 17 (2002) 304–311.

[54] M. Svehla, P. Morberg, W. Bruce, W.R. Walsh, No effect of a type I collagen gel coating in uncemented implant fixation, J. Biomed. Mater. Res. B Appl. Biomater. 74 (2005) 423–428.

[55] N. Bertollo, et al., Effect of surgical fit on integration of cancellous bone and implant cortical bone shear strength for a porous titanium, J. Arthroplasty 26 (2011) 1000–1007.

[56] N. Bertollo, R. Da Assuncao, N.J. Hancock, A. Lau, W.R. Walsh, Influence of electron beam melting manufactured implants on ingrowth and shear strength in an ovine model, J. Arthroplasty 27 (2012) 1429–1436.

[57] W.R. Walsh, N. Bertollo, C. Christou, D. Schaffner, R.J. Mobbs, Plasma-sprayed titanium coating to polyetheretherketone improves the bone-implant interface, Spine J. 15 (2015) 1041–1049.

[58] W.R. Walsh, et al., The in vivo response to a novel Ti coating compared with polyether ether ketone: evaluation of the periphery and inner surfaces of an implant, Spine J. 18 (2018) 1231–1240.

[59] W.R. Walsh, et al., Bone ongrowth and mechanical fixation of implants in cortical and cancellous bone, J. Orthop. Surg. Res. 15 (2020) 1–10.

[60] G.C. Causey, et al., In-Vivo response to a novel pillared surface morphology for osseointegration in an ovine model, J. Mech. Behav. Biomed. Mater. (2021) 104462.

[61] C. Christou, R.A. Oliver, J. Rawlinson, W.R. Walsh, Transdermal fentanyl and its use in ovine surgery, Res. Vet. Sci. 100 (2015) 252–256.